Direct Utilization of Expired Waste Acetaminophen as Organic Anode in Lithium-Ion Batteries

Yonghwan Kim, Seon Jae Hwang, Dohyeong Kim, Jeehye Park, Yoonbin Kim, Junsu Kim, Minjun Bae, Hwichan Hong, Seungman Park, Jungjin Park, Ji Young Maeng, Jaeyeon Lee, Ho Seok Park, Jeongyeon Lee,* and Yuanzhe Piao*

Drug disposal and abuse are increasing every year, and the use of drugs has recently reached its peak due to COVID-19. However, there still remains a lack of awareness regarding the proper disposal of waste medications, and if not properly disposed of, these complex chemical structures can have severe environmental impacts. Furthermore, as this waste contains chemically valuable substances, a recycling strategy is needed. To address this issue, the potential of reusing expired commercial acetaminophen tablets as freeze-dried acetaminophen (FAP) for a lithium-ion battery (LIB) anode material is investigated. The Li storage mechanism and electrochemical performance are investigated via density functional theory, ex situ Fourier-transform infrared spectroscopy, galvanostatic discharge/charge analysis, and cyclic voltammetry. The FAP anode exhibited the excellent electrochemical performances and cycle stability. This study will present a new recycling approach, and the results demonstrate the application potential of waste medications in LIBs, which can contribute to resource recovery and the circular economy.

1. Introduction

Medication use is steadily increasing, and it reached its highest in 2021 because of increased pharmacological interventions to reduce the spread of COVID-19.[1] However, not all of the medications meant for patients are always taken properly, with some being left unused owing to expiration, spillage, or contamination.[2] According to reports, in the United States, 3 to 7% of medications intended for patients are unused, with an estimated cost of 2.4 to 5.4 billion USD.[3,4] The problem of unutilized medication also exists in other parts of the world. In Germany, over 4500 tons of prescription medications are discarded each year, and this value reaches ≈16000 tons for some other countries.[5] Dealing with unused medication is estimated to cost the United Kingdom over 300 million GBP annually.[6]

Unused drugs have severely negative impacts on the environment and the economy. In several nations, unused medications are commonly disposed of via burning or burying.[7,8] Improperly disposed of medications can leak into the soil or water and harm organisms via chemical exposure. Pharmaceutical chemicals originating from poor medication disposal have been detected in the environments of over 71 countries.[9] The German Federal Agency classified the environmental hazards of several pharmaceutical drugs and

Y. Kim, S. J. Hwang, D. Kim, M. Bae, H. Hong, S. Park, J. Park,
J. Y. Maeng, Y. Piao
Department of Applied Bioengineering
Graduate School of Convergence Science and Technology
Seoul National University
Suwon-si, Gyeonggi-do 16229, Republic of Korea
E-mail: parkat9@snu.ac.kr
J. Park
College of Pharmacy
Ewha Womans University
Seoul 03760, Republic of Korea

Y. Kim, J. Kim, H. S. Park
School of Chemical Engineering
Sungkyunkwan University
Suwon 16419, Republic of Korea
J. Lee
Department of Chemistry and Nano Science
Ewha Womans University
Seoul 03760, Republic of Korea
J. Lee
School of Fashion and Textiles
The Hong Kong Polytechnic University
Hung Hom, Kowloon, Hong Kong SAR China
E-mail: jaden-jy.lee@poly.edu.hk
Y. Piao
Advanced Institutes of Convergence Technology
Suwon-si, Gyeonggi-do 16229, Republic of Korea

evaluated the environmental risks associated with the chemicals.[10] Developing a strategy for recycling unused medication is crucial because its improper disposal of medication can harm the environment.

In order to reduce global carbon emissions, there has been an increasing shift towards renewable energy and electric vehicles. In this regard, the lithium-ion battery (LIB), as a critical solution in the carbon-neutral era of modern society, has been widely utilized in various electronic devices, owing to its high energy density and good cycling stability.[11,12] In particular, LIBs have attracted considerable interest as highly promising energy solutions for electric vehicles. With the rapid development of the electric vehicle market, the widespread use of LIBs will result in a high demand for large-scale electrode fabrication, which requires vast amounts of natural resources such as lithium and metal oxides.[13] The recycling or extraction of resources from used LIBs is necessary for preserving the environment and protecting limited natural resources.[14,15] Recycling electrode materials from waste sources promise to be a viable technique for the long-term growth of LIBs. As the main ingredients of medicines are organic compounds with various functional groups, some expired medications can be utilized as LIB electrode materials.[16,17] Various organic electrode materials have been reported as promising alternatives for sustainable energy storage applications in LIBs, owing to their low cost, ease of processing, light weight, and renewability.[18] For example, waste antibiotic tetracycline was directly utilized as an electrode material in LIBs, and it exhibited a specific discharge capacity of 230 mAh g^{-1} at a current density of 0.1 A g^{-1}.[19] Likewise, humic acid extracted from coal and soil was used as an electrode material in LIBs, and it exhibited a specific capacity of 190 mAh g^{-1} at a current density of 0.1 A g^{-1}.[20]

Acetaminophen, commonly sold under the brand names Tylenol or Panadol, is an acetamide compound with various pharmacological properties, such as antipyretic, analgesic, and anti-inflammatory effects.[21] It is widely used as a pain reliever to alleviate common symptoms such as headache and fever.[22] The chemical structure of acetaminophen consists of a benzene ring with one hydroxyl group and an amide nitrogen atom attached to the para position. The chemical structure of acetaminophen that contributes to its pharmacological effects, also enables electrochemical activation by lithium ions through its hydroxyl and carbonyl groups, and provides electrochemical stability owing to the conjugate structure of most of its atoms.[23–26] To the best of our knowledge, no study has investigated the direct utilization of acetaminophen or expired acetaminophen as an LIB anode.

Herein, we utilized freeze-dried acetaminophen (FAP) as an LIB anode material. The freeze-drying process can endow expired commercial acetaminophen tablet with an enhanced surface area and flake-shaped morphology, which facilitate fast electron and Li ion transport. Cyclic voltammetry (CV), ex situ Fourier-transform infrared (FTIR) spectroscopy tests and density functional theory (DFT) were conducted to confirm the reversible lithiation mechanism of FAP. The results showed that the hydroxyl and carbonyl bonds in the amide group of FAP served as lithiation sites. In electrochemical tests, the FAP anode exhibited a reversible capacity of 195.7 mAh g^{-1} at a current density of 1.0 A g^{-1} after 500 cycles and excellent cycling stability. To substantiate the possibility of practical usage, a full-cell was fabricated using a commercial LiFePO$_4$ cathode. The FAP/LiFePO$_4$ full-cell exhibited an initial specific capacity of 157.3 mAh g^{-1} at 0.1 C, which is comparable to the theoretical specific capacity of LiFePO$_4$ (170 mAh g^{-1}). This study demonstrates that the recycling of expired pharmaceuticals as an organic anode offers a great solution to overcome environmental issues caused by pharmaceutical waste disposal.

2. Results and Discussion

2.1. Fabrication and Characterization

Figure 1A illustrates the FAP preparation procedure. To efficiently prepare the slurry for electrode fabrication, expired commercial acetaminophen tablets without any treatment were first ground into bulk acetaminophen powders by using a mortar to increase the solubility of the acetaminophen in water. And this material was denoted as bulk acetaminophen (BAP). Subsequently, the BAP was dispersed in deionized water and freeze-dried for 2 days to obtain fine acetaminophen powders. The acetaminophen easily dissolved in water owing to its hydroxyl and amide functional groups. During the freeze-drying process, ice crystals occupied some spaces between the powder particles, which can increase the surface area after drying.[27] After freeze-drying process, we were able to obtain fine acetaminophen powders without noticeable mass loss (yielding ≈94%, Figure S1, Supporting Information), and this material was denoted as freeze-dried acetaminophen (FAP). To compare the specific surface area of FAP and BAP, we took digital photographs of both samples, with the same mass of 0.2 g, and visually observed them (Figure S2, Supporting Information). The photographs showed a noticeable difference in the specific surface areas of the samples. Furthermore, we calculated the surface areas of the two samples via Brunauer–Emmett–Teller (BET) analysis. FAP exhibited a larger surface area (7.373 m2 g^{-1}) than BAP (1.456 m2 g^{-1}, Figure S3, Supporting Information).

The morphologies of FAP and BAP were characterized via field-emission scanning electron microscopy (FE-SEM) in Figure S4 (Supporting Information). FAP showed a flaky shape and micro-sized particles with various lateral sizes (Figure S4A,B, Supporting Information). The lateral sizes of FAP ranged from 1 to 10 μm, and the average lateral size was ≈5 μm (Figure S5, Supporting Information). Figure S4C,D (Supporting Information) present rock-shaped agglomerated BAP, which corresponded to the BET results. To further investigate the structures of FAP and BAP, transmission electron microscopy (TEM) analysis was conducted (Figure S6, Supporting Information). In Figure S6A,B (Supporting Information), FAP exhibited a very thin flaky shape, with a lateral size of ≈3 μm. Whereas BAP exhibited coarse aggregate morphology (Figure S6C,D, Supporting Information). FAP showed flaky morphology with a larger surface area than BAP, which can enable rapid Li ion and electron transfers.[28] To investigate the elemental composition of FAP, elemental mapping was performed via scanning electron microscopy coupled with energy-dispersive X-ray spectroscopy (SEM-EDX). FAP showed well-distributed C, N, and O elements in the flakes (Figure 1B), consistent with the full X-ray photoelectron spectroscopy (XPS) survey spectra results (**Figure 2**F). The full XPS survey spectra of FAP showed C, N, and O elements, and the atomic percentages of C, N, and O were 74.8%, 4.2%, and 21.2%, respectively (Table S1, Supporting Information). The surface chemical
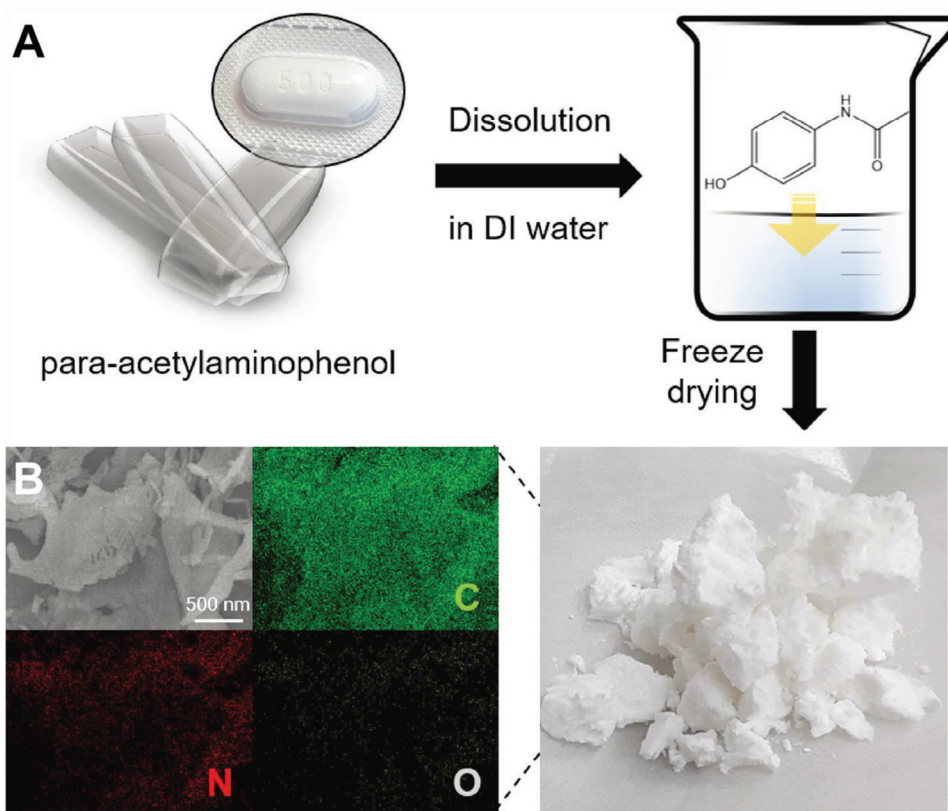
Figure 1. A) Schematic image of synthesis of FAP. B) SEM-EDX mapping of FAP.
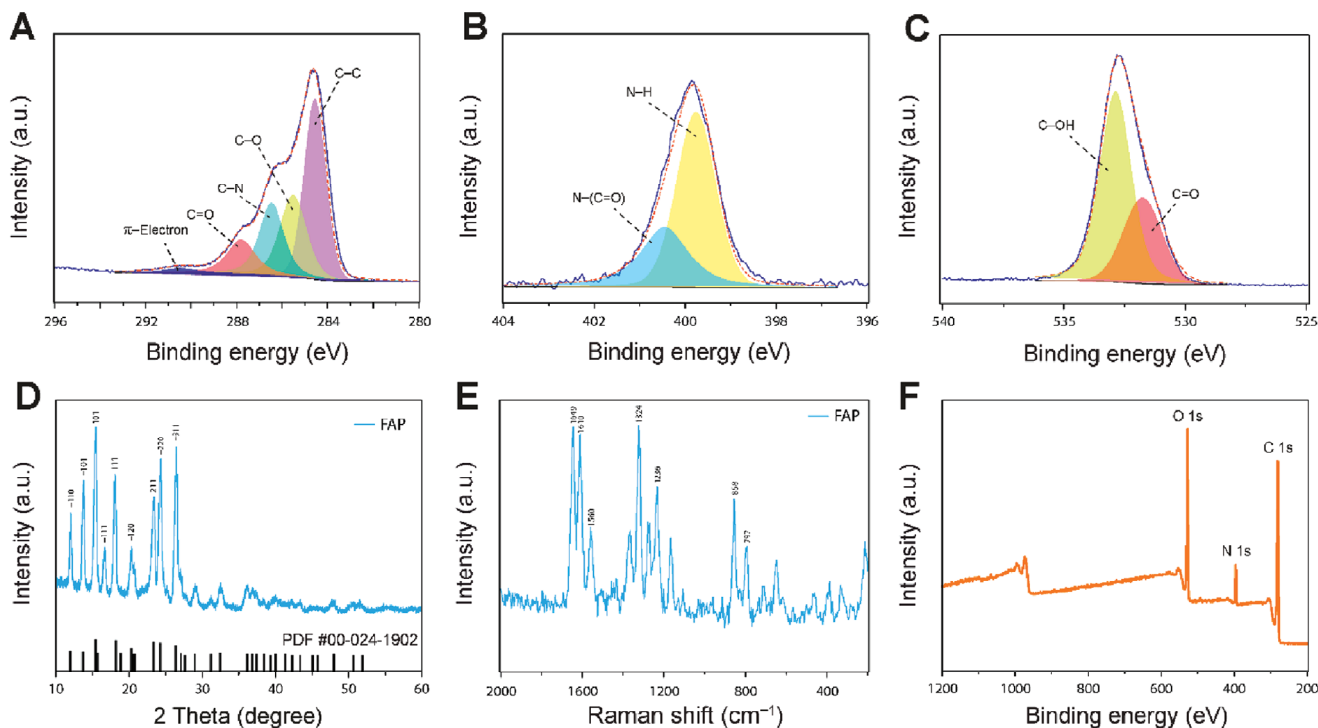
Figure 2. High-resolution XPS spetra of A) C 1s, B) N 1s, and C) O 1s. D) XRD pattern and E) Raman spectra of FAP. F) XPS survey spectra of FAP.
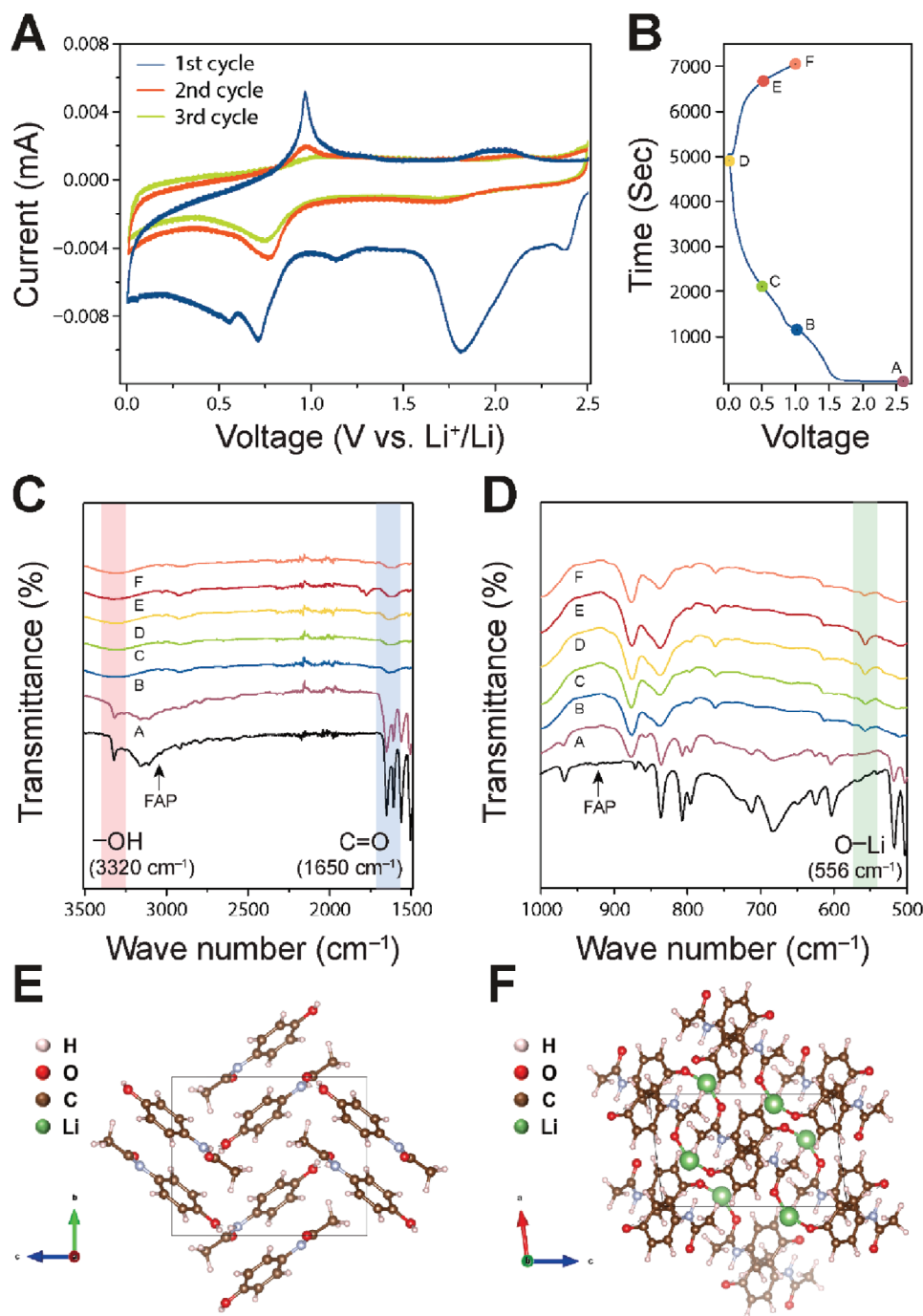
composition of FAP was further investigated via high-resolution XPS. The high-resolution C 1s spectrum (Figure 2A) could be deconvoluted into five characteristic peaks at 284.4, 285.5, 286.5, 287.8, and 290.5 eV, corresponding to carbon atoms in the benzene ring (C—C/C=C), carbon atoms bonded to oxygen via a single bond (C—O), carbon atoms bonded to oxygen via a double bond (C=O), amine (C—N), and a π bond, respectively.[29–31] The carbon atoms bonded to oxygen (C—O, C=O) suggest that the carbon atoms could provide lithiation sites for Li ions.[29,32] The high-resolution N 1s spectrum (Figure 2B) was deconvoluted into two peaks, at 339.8 and 400.5 eV, corresponding to N–H and the amide group (N–C=O).[33] The C=O group in the amide group of FAP provided a lithiophilic site and could undergo intercalation with Li ions to form a C—O—Li bond during lithiation.[29,32] Two deconvoluted peaks at 531.8 and 532.9 eV in the O 1s spectrum corresponded to C=O and C—OH (Figure 2C).[34] The X-ray diffraction patterns of FAP (Figure 2D) showed the nine distinct peaks indicating (−110), (−101), (101), (−111), (111), (−120), (211), (−220), and (−311) crystal phases of the acetaminophen (PDF # 00-039-1503). Figure 2D confirmed the presence of high-purity acetaminophen, without any detectable impurities.

To confirm the preservation of the chemical structure of FAP after the freeze-drying process, Raman spectroscopy, FTIR spectroscopy, and proton nuclear magnetic resonance (^{1}H-NMR) spectroscopy analyses were conducted. The FAP structure was investigated via Raman spectroscopy (Figure 2E). The Raman spectra featured seven distinct peaks, at 1649, 1610, 1560, 1324, 1236, 858, and 797 cm^{-1}, corresponding to ring stretching, amide I, amide II and III stretching, C—C ring stretching, ring breathing, and CNC ring stretching, respectively.[35,36] The FTIR analysis confirmed the chemical structure of FAP (Figure S7, Supporting Information). The distinct peak at 3320 cm^{-1} corresponded to the vibration of the –OH bond in the hydroxyl group, and the broad peaks at ≈3100 cm^{-1} corresponded to the bending vibration of the C–H bond in the –CH$_3$ group.[37] The peaks at 1327, 1369, and 1506 cm^{-1} corresponded to the in-plane symmetric bending and asymmetric bending of the C–H bond. The peaks at 1650, 1562, and 968 cm^{-1} corresponded to the amide I stretching of C=O, amide II bending of N—H, and amide stretching of C—N, respectively.[38] The 1608 cm^{-1} peak corresponded to C=C stretching, while the 1436 cm^{-1} peak corresponded to C—C stretching. The peaks at 837 and 517 cm^{-1} corresponded to the para-disubstituted aromatic ring and out-of-plane ring deformation of phenyl, respectively.[37,39] The chemical characteristics of BAP and FAP were further analyzed via ^{1}H-NMR spectroscopy (Figure S8, Supporting Information). The two signal peaks at 9.64 and 9.14 ppm correspond to the H of the amide group and the hydroxyl group, respectively. The four peaks at 7.34, 7.31, 6.68, and 6.65 ppm correspond to the H of the benzene ring, and the single peak at 1.97 ppm corresponds to the H of the -CH3 group. To verify the stoichiometric ratio of BAP and FAP, the integrated area ratio of the four types of H peaks in the spectra was found to be 1:1:4:3 for both data. This ratio is consistent with the chemical structure of acetaminophen and indicates that both BAP and FAP show high purity without any further purification process. The peaks at 3.34 and 2.50 ppm correspond to H in water and dimethyl sulfoxide-d6 (DMSO-d6) used as solvent. These results demonstrate that the chemical integrity of BAP and FAP is preserved.

2.2. Li Storage Mechanism of FAP

To elucidate the electrochemical reaction kinetics and Li storage mechanism of FAP, we prepared an electrode containing FAP and PVDF at a weight ratio of 7:3 (denoted as FAP-PVDF) to perform a Cyclic voltammetry (CV) test. **Figure 3**A presents the CV curves of FAP-PVDF for the first three cycles at the potential window of 0.001–2.5 V (vs Li^{+}/Li) and a scan rate of 0.1 mV s^{-1}. In the first cathodic scan, five peaks were observed at 2.3, 1.8, 1.13, 0.7, and 0.56 V. The cathodic peaks at ≈2.3, 1.8, and 1.13 V corresponded to the formation of solid electrolyte interphase (SEI) layers, and the peaks disappeared in the subsequent cycles.[20,32,39] The peaks at 0.7 and 0.56 V suggest multiple lithiation steps of FAP. These cathodic peaks of electrochemical reduction indicate that the hydroxyl and carbonyl groups in FAP reacted with Li ions, and O—Li and C—O—Li ionic bonds were formed during the first cathodic reaction.[29,40,41] In addition, these two peaks were gradually weakened over the following cycles, which indicates that the lithiation sites of FAP were gradually activated by Li ions, and subsequently, strong O—Li and C—O—Li bonds were formed. During the anodic scan, a strong anodic peak at 0.97 V and a broad anodic peak at ≈2.0 V were observed, which is consistent with the delithiation process.[29,42] After first CV cycle, following CV cycles closely overlapped, indicating a highly reversible redox reaction of FAP.[51,52]

Ex situ FTIR analysis was employed to detect intermediates at different voltage states and investigate the lithiation/delithiation mechanism of FAP-PVDF during the discharge/charge process. Figure 3B shows the first discharge/charge (lithiation/delithiation) curve of FAP-PVDF, with different voltage states (pristine 2.0 V, lithiated 1.0 V, lithiated 0.5 V, lithiated 0.01 V, delithiated 0.5 V, and delithiated 1.0 V, indicated by points A [brown], B [blue], C [green], D [yellow], E [red], and F [orange], respectively). Figure S9 (Supporting Information) presents the corresponding ex situ FTIR spectra for each voltage states, with the same line colors as in Figure 3B. The FTIR spectra of A–E featured a new peak at 1402 cm^{-1}, which corresponded to the vibration of the PVDF binder (Figure S9, Supporting Information).[43] The 1402 cm^{-1} peak was not detected in the FTIR spectra of FAP, suggesting that the peak was related to the PVDF binder used in FAP-PVDF, and the 1402 cm^{-1} peak was unchanged even after the discharge/charge process. The FTIR spectra were divided into two regions to explain the Li storage mechanism of FAP-PVDF (Figure 3C,D). In the FTIR spectra of A and FAP (Figure 3C), two pronounced peaks at 3320 cm^{-1}, corresponding to –OH vibration, and at 1650 cm^{-1}, corresponding to C=O stretching in the amide group were observed. However, in the FTIR spectra of B–E, the peak disappeared, indicating that the —OH bond and the C=O bond reacted with Li ions when the voltage was changed from 1.0 to 0.01 V.[41] In contrast, a new peak at 556 cm^{-1}, corresponding to the O—Li bond, was observed after the discharge/charge process (Figure 3D).[44] In addition, the intensity of the new peak at 556 cm^{-1} was gradually increased over the discharge process, while it was gradually decreased over the charge process. These observations provide insights into the lithiation/delithiation mechanism of FAP during the discharge/charge process.[53] The disappearance of the —OH and C=O peaks and the

ADVANCED
SCIENCE NEWS

www.advancedsciencenews.com

ADVANCED
MATERIALS
INTERFACES
Open Access

www.advmatinterfaces.de

Figure 3. A) CV curves of FAP-PVDF at 0.1 mV s^{-1}. B) The initial discharge/charge profile of FAP-PVDF at 0.1 A g^{-1}. C) ex situ FTIR spectra of FAP-PVDF at different voltage states in the frequency range of 1500 to 3500 cm^{-1}. D) Ex situ FTIR spectra of FAP-PVDF at different voltage states in the frequency range of 500 to 1000 cm^{-1}. E) Super cell of FAP before lithiation process. F, Super cell of FAP after full lithiation process.

appearance of the O—Li bond peak in the FTIR spectra indicate that −OH and C═O reacted with Li ions and that O—Li bonds were formed.

To further investigate the possible lithiation processes of FAP and to validate the results obtained from CV and ex situ FTIR analyses, density functional theory (DFT) was employed to simulate the lithiation processes of FAP and calculate the binding energy between FAP and Li. The corresponding calculation was shown in experimental section. As illustrated in Figure 3E, within a super cell, four FAP molecules were present, and their molecular structure exhibited herring-bone arrangement, consistent with simulated XRD in Figure S10 (Supporting Information).[57] Each FAP molecule interacted with the others through hydrogen bonds formed between −OH and C═O bond. The DFT

calculations revealed that the interstitial sites between —OH and C═O bond, which are the sources of hydrogen bonds between FAP molecules, were considered to be possible lithiation sites. Figure 3F illustrated four possible equivalent lithiation sites within a super cell. Importantly, Figure S11 and Table S2 (Supporting Information) displayed that as the number of lithiation sites were occupied by Li atoms, the average Li binding energies were decreased to −0.8, −0.95, −1.84, and −2.7 eV. Therefore, each FAP molecule was able to interact with two Li atoms at —OH and C═O bonds. According to the above results of CV, ex situ FTIR and DFT, the lithiation/delithiation mechanism of FAP is depicted in Figure S12 (Supporting Information).

2.3. Electrochemical Performance of FAP Anode

To investigate the electrochemical performances of the FAP anode and BAP anode, we prepared an FAP anode comprised of FAP, Super P, acid-treated multi-walled carbon nanotubes (MWCNTs), and PVDF at a weight ratio of 5:2:2:1 for half-cell tests. Super P and acid-treated MWCNTs were used to enhance electron conductivity.[45] The same method was applied to prepare BAP anode. The electrochemical reaction kinetics of the FAP anode and BAP anode were elucidated via CV. Figure S13 (Supporting Information) presented the CV curves of the FAP anode and BAP anode during the first three cycles at a potential window of 0.001–2.5 V (vs Li$^+$/Li) and a scan rate of 0.1 mV s^{-1}. In the case of FAP anode, the electrochemical behavior of the FAP anode was inconsistent with the CV results of FAP-PVDF (Figure 3A), which is attributable to the high contents of conductive agents (Super P and acid-treated MWCNTs). However, the electrochemical behavior of the FAP anode in the first cathodic cycle (**Figure 4**A) was similar to the CV results for the first cycle of FAP-PVDF. In the first cathodic scan, four peaks were observed at 1.4, 0.92, 0.75, and 0.02 V. The strong cathodic peak at 1.4 V was due to the formation of SEI layers, and this peak disappeared in the curves corresponding to the subsequent cycles.[32] The curve featured small peaks at 0.92 and 0.75 V in the first cathodic cycle, which suggests the lithiation process of FAP. These cathodic peaks indicate that during the first cathodic reaction, hydroxyl and carbonyl bonds in the amide groups of FAP reacted with Li ions, and subsequently, O—Li and C—O—Li ionic bonds were formed. The presence of a strong peak at 0.2 V indicates the occurrence of intercalation between Li and both Super P and acid-treated MWCNTs.[46] During the first anodic scan, broad anodic peaks at 0.01–0.25 V were observed; the peaks corresponded to the deintercalation process of Super P and acid-treated MWCNTs.[47] Notably, the CV curves of subsequent cycles nearly overlapped, indicating the good stability and highly reversible reaction of the FAP anode (Figure S13A, Supporting Information). Similar electrochemical behavior was observed in BAP anode (Figure S13B, Supporting Information). However, FAP anode exhibited significantly enhanced current response compared to BAP anode during the first CV cycle, suggesting that the effect of freeze-drying process increased surface area, enabling rapid transfers of Li ions and electrons.[51,52]

Figure 4B and Figure S14 (Supporting Information) show the initial three and 50th galvanostatic discharge/charge profiles of the FAP and BAP anodes at a current density of 0.5 A g^{-1}, which agree well with the CV results. The first discharge profile featured a plateau at ≈1.5 V, which is related to SEI formation.[32] The sloping plateau starting at ≈0.9 V in the following discharge profiles is attributed to the lithiation process of FAP and BAP anodes. These results are consistent with the first cathodic process described by the CV curves in Figure 4A. The first-cycle discharge and charge capacities were 550 and 201 mAh g^{-1}, respectively, and the initial coulombic efficiency was 36.5%. During the initial discharge/charge process, the irreversible capacity loss is attributed to the formation of an initial irreversible SEI film, which is a typical characteristic of organic anodes.[48,49,62,63] The coulombic efficiency following 2nd and 50th cycles exhibited 95.7 and 98.8%. These results indicate that the FAP anode was gradually stabilized after the first cycle.

The rate performance of the FAP and BAP anodes was evaluated according to the discharge/charge process at various current densities from 0.1 to 5 A g^{-1} (Figure 4C; Figure S15, Supporting Information). The average reversible discharge/charge capacities of the FAP anode at current densities of 0.1 A g^{-1} were 232.4 mAh g^{-1} which is significantly higher than that of the BAP anode (181.7 mAh g^{-1}). More importantly, FAP anode exhibits 198.7, 185.0, 162.1, and 113.1 mAh g^{-1} at each current density of 0.2, 0.5, 1, 2, and 5 A g^{-1}, respectively, indicating much better rate performance than BAP anode (162.8, 149.1, 125.9, 96.6, and 66.8 mAh g^{-1} at each current density of 0.2, 0.5, 1, 2, and 5 A g^{-1}). When the current density was returned to 0.1 A g^{-1}, the FAP anode exhibited a reversible capacity of 210.7 mAh g^{-1}, demonstrating the fast kinetics of the FAP anode. The cycle performances of the FAP anode at current densities of 0.5 and 1 A g^{-1} for 500 cycles are shown in Figure 4D. In the first cycle, the FAP anode exhibited specific capacities of 156.1 and 97.6 at 0.5 and 1 A g^{-1}, respectively. However, from the second cycle, as the number of cycles increased, the specific discharge capacity gradually increased without decay, and the values after 500 cycles were 266.7 and 195.7 mAh g^{-1} at current densities of 0.5 and 1 A g^{-1} respectively.

Electrochemical Impedance Spectroscopy (EIS) was conducted to track the gradual increasing of specific capacity of the FAP anode during cycling. FAP anodes were performed a series of cycles, including 1, 2, 3, 5, 10, and 100 cycles at 0.5 A g^{-1}, to measure the charge transfer resistance (R_{ct}). The Nyquist plots of the FAP anode were shown in Figure S16 (Supporting Information). During the first 2 cycles, we observed a gradual increase in R_{ct} value from 493 to 737 Ω, attributed to the formation of the SEI film. However, after 3 cycles, R_{ct} value began to decrease, reaching values of 383, 330, 196, and 43.6 Ω at 3rd, 5th, 10th, and 100th cycle, respectively. This decrease indicated gradual activation and stabilization of the FAP anode resulting in improved electrochemical contact and charge transfer during cycling.[60]

FE-SEM was further employed to investigate the morphology changes of pristine and cycled FAP anodes. As shown in Figure S17A,B, (Supporting Information) the pristine FAP anode exhibited a homogeneous distribution of conductive agents (Super P and acid-treated MWCNTs) on FAP flakes, with FAP flakes measuring 1−2 µm in size clearly observed in the electrode. After 50 cycles at current density 1 A g^{-1}, the FAP anode (Figure S17C,D, Supporting Information) remained remarkably stable, with FAP flakes still present. Notably, these FAP flakes were observed to be covered with nanoparticles ranging in size from 20−30 nm, along with conductive agents. This phenomenon can be attributed to
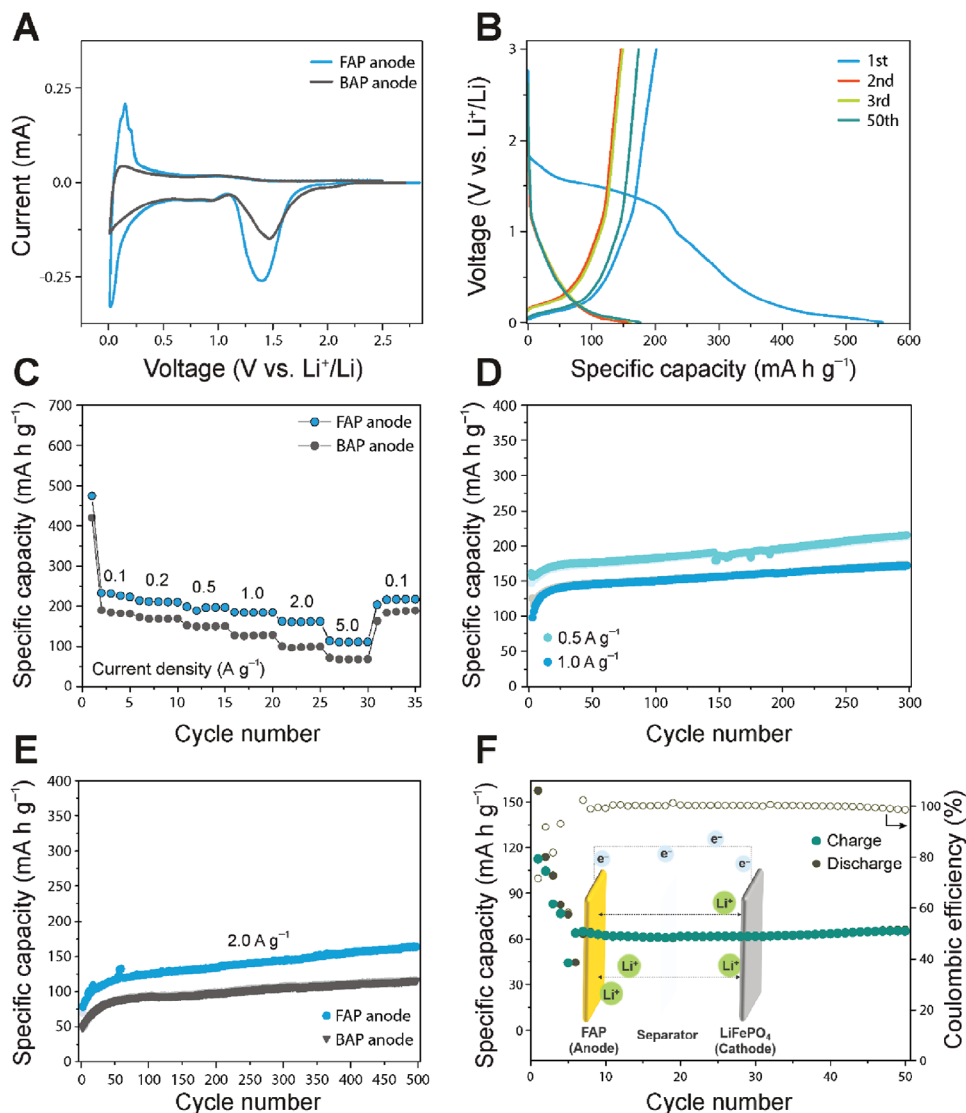
Figure 4. A) The 1st CV curves of FAP anode and BAP anode at 0.1 mV s^{-1}. B) The 1st, 2nd, 3rd, and 50th galvanostatic discharge/charge profile of FAP anode at 0.5 A g^{-1}. C) Rate performance of FAP anode and BAP anode at different current densities. D) Cycle performances of FAP anode at 0.5 and 1.0 A g^{-1}. E) Cycle performances of FAP anode and BAP anode at 2.0 A g^{-1}. F) Cycle performance and coulombic efficiency of FAP/LiFePO$_4$ full-cell at 0.5 C.

the break-down of FAP during cycling and these nanoparticles would improve the redox reaction and facilitate fast Li ion and electron transfer.[61] As a result, the gradual increase in specific capacity for both anodes can be attributed to the gradual activation of the electrode materials with increased active sites upon cycling and/or to the gradual increase in the interfacial Li storage capacity.[20] In order to compare cycle stability of FAP and BAP anodes at high current density, as shown in Figure 4E, the cycle performances of both anodes at current density of 2 A g^{-1} for 500 cycles were conducted. In Figure 4E, the FAP anode exhibited initial specific capacity of 78.6 mAh g^{-1} and the specific capacity gradually increased to 162.9 mAh g^{-1}. Comparatively, the BAP anode showed initial specific capacity 48.6 mAh g^{-1} and gradually increased to 116.1 mAh g^{-1}, which were lower than those of the FAP anode. To further investigate the electrochemical kinet-

ics of the FAP anode, CV analysis was conducted at a scan rate of 0.1 to 0.5 mV s^{-1} (Figure S18A, Supporting Information). The linear fit of the logarithmic relationship between the scan rate and the peak current is shown in Figure S18B (Supporting Information). The slope values of peaks 1 and 2 were 0.735 and 0.705, respectively. These values demonstrate that the Li storage capacity of the FAP anode was controlled by the capacitance behavior, leading to fast Li ion insertion and extraction.[50]

To verify the practical application of the FAP anode, we fabricated a Li ion full-cell using the pre-lithiated FAP anode. The anode was paired with the LiFePO$_4$ cathode to investigate the electrochemical performance of the full-cell. Before the full-cell was prepared, the FAP anode was galvanostatically pre-lithiated five times at 0.01–1.0 V in the half-cell (vs Li$^+$/Li) at a current density of 0.1 A g^{-1} and then discharged to a cut-off

voltage of 0.01 V (Figure S19, Supporting Information). The discharge/charge curves of the FAP/LiFePO4 full-cell during the first cycle at the potential range of 2.0–4.0 V (vs Li$^+$/Li) and a current density of 0.1 C are presented in Figure S20 (Supporting Information). The cell exhibited an initial discharge capacity of 157.3 mAh g^{-1}, which is comparable to the theoretical specific capacity of LiFePO$_4$ (170 mAh g^{-1}). The cycling performance of the FAP/LiFePO$_4$ full-cell at 0.5 C for 50 cycles is shown in Figure 4F. The FAP/LiFePO$_4$ full-cell showed specific capacities of 157.3 and 113.9 mAh g^{-1} at 0.1 C after one and two cycles, respectively. Decreasing in specific capacity during the first and second cycles, at a current density of 0.1 C, can be attributed primarily to the formation of the SEI layer. Formation of SEI layer may consume lithium ions, leading to an initial capacity loss.[62] After the 50 cycles at 0.5 C, the specific capacity of the FAP/LiFePO$_4$ exhibited a specific capacity of 63.1 mAh g^{-1} and showed a stable coulombic efficiency of ≈99.9% without noticeable capacity decay indicating stability of FAP. The discharge/charge curves at different cycles further prove the electrochemical stability and low polarization (Figure S21, Supporting Information). According to the above results, the FAP/LiFePO$_4$ full-cell showed good cycling stability, making it suitable for practical LIB applications.

3. Conclusion

We directly reused an expired commercial acetaminophen tablet as a LIB anode by using a facile freeze-drying method to retain the higher surface area and the homogeneous mixing with conducting agents. As-prepared FAP anodes were tested to confirm the electrochemical performances for LIB anodes. Our results exhibited the excellent rate and cycle performances and good stability. We then conducted the ex situ FTIR analysis with different voltage states to prove their redox reaction. DFT calculation was also employed to calculate binding energies of Li atoms to FAP and prove favorable lithiation mechanism. It was proven that FAP anodes facilitated the highly reversible lithiation/delithiation mechanism during the discharge/charge process. Furthermore, we fabricated the FAP/LiFePO$_4$ full cells, which showed the reasonable cyclic performances for 50 cycles at 0.5 C. We believe that this study can demonstrate the first step towards reducing waste on Earth and reusing it as a new source of energy in the future. However, further studies on optimization are required for more practical applications.

4. Experimental Section

Materials Preparation: Expired commercial acetaminophen tablets were obtained directly from a pharmacy. Sulfuric acid (H$_2$SO$_4$, 95%) and nitric acid (HNO$_3$, 68.0%–70.0%) were purchased from Samchun Chemicals Co. Deionized water was obtained using a Milli-Q ultrapure water system (Millipore, USA). MWCNTs were obtained from Sigma Aldrich Co. MWCNTs were refluxed in a H$_2$SO$_4$ and HNO$_3$ mixture (3:1, v/v) for 3 h at 60 °C to prepare acid-treated MWCNTs.

Synthesis of FAP: First, the expired commercial acetaminophen tablet was ground into bulk acetaminophen powder (BAP). The BAP was then dispersed in 50 mL of deionized water under sonication for 1 h and freeze-dried for 2–3 days to obtain FAP.

Materials Characterization: The morphologies of FAP and BAP were characterized using a field-emission scanning electron microscope (Hi-tachi S-4800) equipped with an energy-dispersive X-ray spectrometer. Further morphology characterization was performed via TEM (JEOL JEM-2100F, 200 keV). BET N$_2$ adsorption/desorption analysis was conducted using a BELSORP-mini II (MicrotracBEL). The crystal structure of the sample was characterized using an X-ray diffractometer (Bruker New D8 Advance) with Cu Kα (α = 1.5406 Ω) radiation. XPS analysis (AXIS-HIS, Kratos Analytical) was conducted using a Mg Kα X-ray source. FTIR measurements were performed on a Nicolet 5700 spectrometer in the attenuated total reflection mode. To perform the ex situ FTIR analysis, an electrode containing FAP and PVDF at a weight ratio of 7:3 (FAP-PVDF) was prepared at various charge states, including pristine, discharge to 1.0 V, discharge to 0.5 V, discharge to 0.01 V, recharge to 0.5 V, and recharge to 1.0 V. The electrode was then measured on the Nicolet 5700 spectrometer. The Raman spectrum was obtained using a Raman spectrometer (DXR2xi Raman Imaging Microscope, Thermo Scientific) with an excitation laser wavelength of 532 nm. The ^{1}H NMR spectra were recorded on a Bruker AVANCE III 400 MHz spectrometer (^{1}H 400 MHz) in DMSO-d$_6$.

Electrochemical Test: For the half-cell test, FAP (or BAP), Super P, acid-treated MWCNTs, and PVDF in N-methyl pyrrolidone were mixed via ball milling at a weight ratio of 5:2:2:1 to form a homogeneous slurry. The well-dispersed FAP slurry was cast onto the copper foil using a doctor blade. The electrode was oven-dried at 60 °C for 12 h and cut using a punching machine with an 11 mm diameter. The areal mass loadings of the FAP anode were ≈0.6–0.7 mg cm^{-2}. The electrochemical performance was tested with a CR-2016 coin cell using Li metal as the counter electrode and a Celgard 2450 membrane as the separator. The electrolyte was 1.3 M LiPF$_6$ in a 3:7 (v/v) mixture of ethylene carbonate and diethyl carbonate with 10 wt.% fluoroethylene carbonate. Galvanostatic electric discharge/charge tests were performed at different current densities and a voltage range of 0.001–2.5 V (vs Li$^+$/Li).

For the full-cell test, a LiFePO$_4$ cathode was prepared by mixing LiFePO$_4$, Super P, and PVDF in N-methyl pyrrolidone at a weight ratio of 7:1.5:1.5. The homogeneous slurry was cast on an Al foil and dried at 60 °C for 12 h and cut using a punching machine with an 11 mm diameter. The mass loading of LiFePO$_4$ was ≈2.5 mg cm^{-2}. The pre-lithiated FAP anode was fabricated by pre-lithiating the FAP anode five times between 0.01 and 1.0 V in the half-cell (vs Li$^+$/Li) at a current density of 0.1 A g^{-1} and then discharged to a cut-off voltage of 0.01 V. The electrochemical performance was tested with a CR-2016 coin cell using LiFePO$_4$ as a cathode and pre-lithiated FAP as an anode. The separator was a Celgard 2450 membrane. The electrolyte was 1.3 M LiPF$_6$ in a 3:7 (v/v) mixture of ethylene carbonate and diethyl carbonate with 10 wt.% fluoroethylene carbonate. Galvanostatic electric discharge/charge tests were performed at a voltage range of 2.0–4.0 V (vs Li$^+$/Li). The CV test was conducted at 0.001–2.5 V (vs Li$^+$/Li) and a scan rate of 0.1 to 0.5 mV s^{-1}. CV and galvanostatic tests were performed using a WBCS3000S cycler (WonATech Co.). Electrochemical impedance spectroscopy was performed using a ZIVE SP1 electrometer (ZIVE LAB, WonATech Co.). The coin cell was assembled in an argon-filled glove box with moisture and oxygen contents of <0.1 ppm.

Computational Methods: All computational calculations were achieved by the density functional theory (DFT) in Quantum Espresso package version 7.1 with Perdew-Burke-Ernzerhof (PBE) exchange correlation functional.[54,55] Pseudopotentials were selected at the standard solid-state pseudopotential library (SSSP efficiency).[56] A monoclinic cell accommodating four units of FAP molecule was relaxed.[57] Total energy and force convergence threshold were 1×10^{-4} Ry and 1×10^{-3} Ry/Bohr, respectively. The structural relaxation was carried out with the wave function cutoff of 50 Ry at a single gamma point calculation. The final energy was calculated at 60 Ry with a gamma-point-centered $3 \times 3 \times 3$ Monkhorst-Pack grid.[58] Electronic self-consistent field step convergence threshold was 1.0e-8 for both relaxation and final energy calculations. Mazari-Vanderbilt smearing of 0.02 Ry was employed.[59] The average binding energy between FAP and lithium atom is calculated with equation:

$$\Delta E_{binding} = (E_{substrate} - nLi - E_{substrate} - nELi)/n \qquad (1)$$

where n is number of lithium atom.

Supporting Information

Supporting Information is available from the Wiley Online Library or from the author.

Conflict of Interest

The authors declare no conflict of interest.

Data Availability Statement

The data that support the findings of this study are available from the corresponding author upon reasonable request.

[1] D. Dadiomov, R. Trotzky-Sirr, A. Shooshtari, D. M. Qato, *Drug Alcohol Depend.* **2022**, *232*, 109291.
[2] M. Mutaseim, A. H. Mohamed, A. Ahmed, H. Furqan, *Pharmacy* **2019**, *17*, 61.
[3] S. Doyle, *CMAJ* **2010**, *182*, E197.
[4] A. V. Law, P. Sakharkar, A. Zargarzadeh, B. W. B. Tai, K. Hess, M. Hata, R. Mireles, C. Ha, T. J. Park, *Res. Soc. Adm. Pharm.* **2015**, *11*, 571.
[5] T. J. Scheytt, P. Mersmann, T. Heberer, *J. Contam. Hydrol.* **2006**, *83*, 53.
[6] Y. Luo, Z. Wan, *J. Cleaner Prod.* **2022**, *376*, 134304.
[7] L. Tischler, M. Buzby, D. S. Finan, V. L. Cunningham, *Integr. Environ. Assess. Manage.* **2013**, *9*, 142.
[8] S. M. Hanning, C. Hua, S. Baroutian, R. Burrell, M. Taylor, L. J. Wright, D. Svirskis, *J. Mater. Cycles Waste Manage.* **2022**, *24*, 1603.
[9] T. Aus Der Beek, F.-A. Weber, A. Bergmann, S. Hickmann, I. Ebert, A. Hein, A. Küster, *Environ. Toxicol. Chem.* **2016**, *35*, 823.
[10] A. Küster, N. Adler, *Philos. Trans. R. Soc., B* **2014**, *369*, 20130587.
[11] J. Han, *Environ. Chem. Lett.* **2022**, *20*, 2989.
[12] A. El Kharbachi, O. Zavorotynska, M. Latroche, F. Cuevas, V. Yartys, M. Fichtner, *J. Alloys Compd.* **2020**, *817*, 153261.
[13] B. Huang, Z. Pan, X. Su, L. An, *J. Power Sources* **2018**, *399*, 274.
[14] J. Piatek, S. Afyon, T. M. Budnyak, S. Budnyk, M. H. Sipponen, A. Slabon, *Adv. Energy Mater.* **2021**, *11*, 2003456.
[15] J. Kim, Y. Kim, J. Yoo, G. Kwon, Y. Ko, K. Kang, *Nat. Rev. Mater.* **2023**, *8*, 54.
[16] H. Hou, Z. Dai, X. Liu, Y. Yao, C. Yu, D. Li, *Front Mater.* **2019**, *6*, 80.
[17] Z. Dai, H. Hou, X. Liu, Y. Yao, Q. Liao, C. Yu, D. L. Li, *Waste Biomass Valorization* **2020**, *11*, 357.
[18] Y. Liang, Z. Tao, J. Chen, *Adv. Energy Mater.* **2012**, *2*, 742.
[19] H. Hou, Z. Dai, X. Liu, Y. Yao, Q. Liao, C. Yu, D. L. Li, *Sci. Total Environ.* **2018**, *630*, 495.
[20] H. Zhu, J. Yin, X. Zhao, C. Wang, X. Yang, *Chem. Commun.* **2015**, *51*, 14708.
[21] J. E. Sullivan, H. C. Farrar, *Pediatrics* **2011**, *127*, 20103852.
[22] D. L. Simmons, D. Wagner, K. Westover, *Clin. Infect. Dis.* **2000**, *31*, S211.
[23] H. Ke, Q. Zhang, X. Zhang, G. Cheng, Y. Sun, J. Li, H. Cheng, *Mater. Lett.* **2021**, *286*, 129235.
[24] F. Zhang, M. Wu, X. Wang, Q. Xiang, Y. Wu, J. Ding, Y. Sun, *Chem. Eng. J.* **2023**, *457*, 141335.
[25] L. Bai, Q. Gao, Y. Zhao, *J. Mater. Chem. A* **2016**, *4*, 14106.
[26] J. Wu, X. Rui, G. Long, W. Chen, Q. Yan, Q. Zhang, *Angew. Chem., Int. Ed.* **2015**, *54*, 7354.
[27] G. Lian, C.-C. Tuan, L. Li, S. Jiao, Q. Wang, K.-S. Moon, D. Cui, C.-P. Wong, *Chem. Mater.* **2016**, *28*, 6096.
[28] H. Shen, Y. Huang, R. Hao, Y. Chang, Z. Ma, B. Guo, P. Wang, H. Yang, J. Cheng, Q. Li, H. Wang, Z. Liu, A. Nie, *ACS Sustainable Chem. Eng.* **2020**, *8*, 17597.
[29] J. Du, J. Ren, M. Shu, X. Xu, Z. Niu, W. Shi, R. Si, P. Cheng, *Angew. Chem., Int. Ed.* **2021**, *60*, 4142.
[30] Z. Chen, P. Sun, P. Bai, H. Su, J. Yang, Y. Liu, Y. Xu, Y. Geng, *Chem. Commun.* **2021**, *57*, 10791.
[31] J. Moon, J. Y. Jeong, J. I. Kim, S. Kim, J. H. Park, *J. Power Sources* **2019**, *416*, 89.
[32] S. Li, J. Lin, Y. Zhang, S. Zhang, T. Jiang, Z. Hu, J. Liu, D.-Y. Wu, L. Zhang, Z. Tian, *Adv. Energy Mater.* **2022**, *12*, 2201347.
[33] T. B. Schon, S. Y. An, A. J. Tilley, D. S. Seferos, *ACS Appl. Mater. Interfaces* **2019**, *11*, 1739.
[34] F.-M. Wang, K. Wagari Guji, A. Ramar, L. Merinda, W.-C. Chien, *ACS Sustainable Chem. Eng.* **2021**, *9*, 12286.
[35] A. Luczak, L. J. Jallo, R. N. Dave, Z. Iqbal, *Powder Technol.* **2013**, *236*, 52.
[36] J. F. Kauffman, L. M. Batykefer, D. D. Tuschel, *J. Pharm. Biomed. Anal.* **2008**, *48*, 1310.
[37] F. Zapata, A. López-Fernández, F. Ortega-Ojeda, G. Quintanilla, C. García-Ruiz, G. Montalvo, *J. Chem. Educ.* **2021**, *98*, 2675.
[38] B. Liu, X. Han, Z. Wang, H. Zhang, N. Liu, X. Gao, J. Gao, A. Zheng, *J. Drug Delivery Sci. Technol.* **2021**, *66*, 102855.
[39] H. Sonoki, M. Matsui, N. Imanishi, *J. Electrochem. Soc.* **2019**, *166*, A3593.
[40] X. Yang, Z. Liu, X. Chen, W. Wang, X. Chen, Z. Yuan, H. Zhou, R. Zeng, Y. Luo, *J. Electroanal. Chem.* **2016**, *782*, 202.
[41] L. Zhai, G. Li, X. Yang, S. Park, D. Han, L. Mi, Y. Wang, Z. Li, S.-Y. Lee, *Adv. Funct. Mater.* **2022**, *32*, 2108798.
[42] C. Ma, X. Zhao, L. Kang, K.-X. Wang, J.-S. Chen, W. Zhang, J. Liu, *Angew. Chem., Int. Ed.* **2018**, *57*, 8865.
[43] X. Huang, W. Wang, Y. Liu, H. Wang, Z. Zhang, W. Fan, L. Li, *Chem. Eng. J.* **2015**, *273*, 421.
[44] M. Armand, S. Grugeon, H. Vezin, S. Laruelle, P. Ribière, P. Poizot, J.-M. Tarascon, *Nat. Mater.* **2009**, *8*, 120.
[45] S. Zhang, S. Ren, D. Han, M. Xiao, S. Wang, L. Sun, Y. Meng, *ACS Appl. Mater. Interfaces* **2020**, *12*, 36237.
[46] J. Zhang, Z. Xie, W. Li, S. Dong, M. Qu, *Carbon* **2014**, *74*, 153.
[47] P. Wu, G. Shao, C. Guo, Y. Lu, X. Dong, Y. Zhong, A. Liu, *J. Alloys Compd.* **2019**, *802*, 620.
[48] T. Gu, M. Zhou, B. Huang, S. Cao, J. Wang, Y. Tang, K. Wang, S. Cheng, K. Jiang, *Chem. Eng. J.* **2019**, *373*, 501.
[49] S. Liu, H. Hou, W. Hu, X. Liu, J. Duan, R. Meng, *RSC Adv.* **2016**, *6*, 3742.

[50] W. Ren, H. Zhang, C. Guan, C. Cheng, *Adv. Funct. Mater.* **2017**, *27*, 1702116.

[51] Y. Ouyang, H. Ye, X. Xia, X. Jiao, G. Li, S. Mutahir, L. Wang, D. Mandler, W. Lei, Q. Hao, *J. Mater. Chem. A* **2019**, *7*, 3228.

[52] C. Zhang, L. Wang, W. Lei, Y. Wu, C. Li, M. A. Khan, Y. Ouyang, X. Jiao, H. Ye, S. Mutahir, Q. Hao, *Mater. Lett.* **2019**, *234*, 21.

[53] S. Mutahir, C. Wang, J. Song, L. Wang, W. Lei, X. Jiao, M. A. Khan, B. Zhou, Q. Zhong, Q. Hao, *Appl. Mater. Today* **2020**, *21*, 100813.

[54] P. Giannozzi, S. Baroni, N. Bonini, M. Calandra, R. Car, C. Cavazzoni, D. Ceresoli, G. L. Chiarotti, M. Coccocioni, I. Dabo, A. Dal Corso, S. De Gironcoli, S. Fabris, G. Fratesi, R. Gebauer, U. Gerstmann, C. Gougoussis, A. Kokalj, M. Lazzeri, L. Martin-Samos, N. Marzari, F. Mauri, R. Mazzarello, S. Paolini, A. Pasquarello, L. Paulatto, C. Sbraccia, S. Scandolo, G. Sclauzero, A. P. Seitsonen, et al., *J. Phys.: Condens. Matter* **2009**, *21*, 395502.

[55] P. Giannozzi, O. Andreussi, T. Brumme, O. Bunau, M. Buongiorno Nardelli, M. Calandra, R. Car, C. Cavazzoni, D. Ceresoli, M. Coccocioni, N. Colonna, I. Carnimeo, A. Dal Corso, S. De Gironcoli, P. Delugas, R. A. Distasio, A. Ferretti, A. Floris, G. Fratesi, G. Fugallo, R. Gebauer, U. Gerstmann, F. Giustino, T. Gorni, J. Jia, M. Kawamura, H.-Y. Ko, A. Kokalj, E. Küçükbenli, M. Lazzeri, et al., *J. Phys.: Condens. Matter* **2017**, *29*, 465901.

[56] G. Prandini, A. Marrazzo, I. E. Castelli, N. Mounet, N. Marzari, *npj Comput. Mater.* **2018**, *4*, 72.

[57] D. Y. Naumov, M. A. Vasilchenko, J. A. K. Howard, *Acta Crystallogr., Sect. C: Struct. Chem.* **1998**, *54*, 653.

[58] H. J. Monkhorst, J. D. Pack, *Phys. Rev. B* **1976**, *13*, 5188.

[59] N. Marzari, D. Vanderbilt, A. De Vita, M. C. Payne, *Phys. Rev. Lett.* **1999**, *82*, 3296.

[60] Y. Wang, W. Liu, R. Guo, Q. Qu, H. Zheng, J. Zhang, Y. Huang, *J. Mater. Chem. A* **2019**, *7*, 22621.

[61] C. Zhang, W. Hu, H. Jiang, J.-K. Chang, M. Zheng, Q.-H. Wu, Q. Dong, *Electrochim. Acta* **2017**, *246*, 528.

[62] B. Liu, K. Zhu, K. Ye, J. Yan, G. Wang, D. Cao, *J. Power Sources* **2022**, *552*, 232226.

[63] Y. Wang, Y. Deng, Q. Qu, X. Zheng, J. Zhang, G. Liu, V. S. Battaglia, H. Zheng, *ACS Energy Lett.* **2017**, *2*, 2140.